Top-illuminated dye-sensitized solar cells with a room-temperature-processed ZnO photoanode on metal substrates and a Pt-coated Ga-doped ZnO counter electrode

2011 J. Phys. D: Appl. Phys. 44 045102

(http://iopscience.iop.org/0022-3727/44/4/045102)

IOP PUBLISHING JOURNAL OF PHYSICS D: APPLIED PHYSICS

J. Phys. D: Appl. Phys. **44** (2011) 045102 (8pp) doi:10.1088/0022-3727/44/4/045102

Top-illuminated dye-sensitized solar cells with a room-temperature-processed ZnO photoanode on metal substrates and a Pt-coated Ga-doped ZnO counter electrode

A K K Kyaw[1,2], X W Sun[1,3,5], J L Zhao[1,3], J X Wang[1], D W Zhao[1], X F Wei[2], X W Liu[2], H V Demir[1,2,4,5] and T Wu[2]

[1] School of Electrical and Electronic Engineering, Nanyang Technological University, 50 Nanyang Avenue, Singapore 639798, Singapore
[2] School of Physical and Mathematical Science, Nanyang Technological University, 21 Nanyang Link, Singapore 637371, Singapore
[3] Department of Applied Physics, Tianjin University, Tianjin 300072, People's Republic of China
[4] Department of Electrical and Electronic Engineering and Department of Physics, Bilkent University, Bilkent, 06800 Ankara, Turkey

E-mail: exwsun@ntu.edu.sg and hvdemir@ntu.edu.sg

Received 21 October 2010, in final form 23 November 2010
Published 11 January 2011
Online at stacks.iop.org/JPhysD/44/045102

Abstract

We report on top-illuminated, fluorine tin oxide/indium tin oxide-free (FTO/ITO-free), dye-sensitized solar cells (DSCs) using room-temperature-processed ZnO layers on metal substrates as the working electrodes and Pt-coated Ga-doped ZnO layers (GZO) as the counter electrodes. These top-illuminated DSCs with GZO render comparable efficiency to those employing commercial FTO counter electrodes. Despite a lower current density, the top-illuminated DSCs result in a higher fill factor than conventional DSCs due to a low ohmic loss at the electrode/semiconductor interface. The effect of metal substrate on the performance of the resulting top-illuminated DSCs is also studied by employing various metals with different work functions. Ti is shown to be a suitable metal to be used as the working electrode in the top-illuminated device architecture owing to its low ohmic loss at the electrode/semiconductor interface, minimum catalytic activity on redox reactions and high resistance to corrosion by liquid electrolytes.

(Some figures in this article are in colour only in the electronic version)

1. Introduction

Dye-sensitized solar cells (DSCs) provide a promising alternative to conventional silicon photovoltaic technology thanks to their high photon-to-electricity conversion efficiency (over 11%) [1], low-cost and environmentally friendly manufacturing from abundant and non-toxic materials such as TiO_2 and ZnO photoanodes. Current state-of-the-art DSCs are typically fabricated on a fluorine tin oxide (FTO) glass, allowing the light to enter from the bottom of the glass substrate. However, it is estimated that conducting glass is the most expensive part of a DSC and it incurs 60% of the total cost [2]. Moreover, a relatively high sheet resistance of the conducting glass compared with metal is another obstacle to producing large-area solar cells. Therefore, alternatively, top-illuminated DSCs are particularly attractive because they can be fabricated on inexpensive opaque substrates such as

[5] Authors to whom any correspondence should be addressed.

metal foils or plastic foils with metal coatings which may possibly lead to low-cost, light-weight and flexible DSC fabrication through roll-to-roll manufacturing. Moreover, in the case of a DSC with TiO_2 nanotube array grown from the anodization of Ti metal, top-illuminated configuration allows us to assemble the DSC directly on the Ti metal foil [3], eliminating the expensive and time-consuming sputtering process to deposit Ti film on the conducting glass [4] or lift-off and attachment processes to transfer the nanocrystalline film from the opaque substrate to the FTO glass [5, 6]. Because of these advantages, top-illuminated DSCs with various metal substrates were demonstrated by several groups [7–10] and the highest efficiency of 7.2% has been achieved using a sintered nanocrystalline TiO_2 photoanode and a Pt-coated ITO counter electrode [10].

However, in such a top-illuminated DSC, TiO_2 layer is sintered at high temperatures (450–500 °C) to improve the connection between TiO_2 particles. Despite the capability of withstanding a high temperature, sintering at a high temperature oxidizes the metal substrate due to oxygen in ambient air or diffusion of oxygen from metal oxide semiconductor, reducing the conductivity of the electrode. An additional sputtered indium tin oxide (ITO) layer on top of the metal substrate and a blocking layer between ITO and the metal substrate are required to further improve the efficiency [7]. Hence, a surface activation method which does not require high-temperature sintering yet provides good interconnection between particles and substrate adhesion is essential. A room-temperature fabrication not only facilitates the manufacturing of solar cells but also saves energy during fabrication. On the other hand, a Pt-coated ITO or FTO glass is widely used as the counter electrode in the top-illuminated DSCs [3, 7–10]. Nevertheless, the addictive use of ITO, especially for the production of transparent electrodes for large-area photovoltaic devices, is endangered by the scarcity and ever-increasing price of indium [11]. Similarly, the quality of FTO films available for industrial photovoltaic production is not ideal because high-quality FTO is only available at a laboratory scale due to process restraints and low production volume [12, 13]. This situation drives the search for alternative transparent conducting materials as the counter electrode to replace ITO and FTO.

In order to address the limitations discussed above, herein we report on a new class of FTO/ITO-free top-illuminated DSCs employing room-temperature-processed porous ZnO films as the photoanode and Pt-coated Ga-doped ZnO (GZO) films as the counter electrode. The photoanodes are prepared at room temperature by squeegee-printing a paste of ZnO nanoparticles (NPs). Zinc-acetate-assisted inter-particle connection and ammonia activation ensure a good interconnection between particles and substrate adhesion, avoiding the need for high-temperature sintering. Instead of typical FTO/ITO counter electrode, GZO which has been applied as a transparent electrode in organic solar cells [14] and conventional DSCs [15] is adopted in this work for its low cost, natural abundance, non-toxicity and high thermal/chemical stability [16, 17]. We demonstrate that the performance of these DSCs with GZO is comparable to that of DSCs with FTO counter electrodes. The photovoltaic characteristics of these bottom- and top-illuminated devices are compared and the differences are discussed in terms of optical transmittance spectrum, incident photon-to-current efficiency (IPCE) and energy band diagram. The influence of metal substrate on the photovoltaic properties of the resulting devices is also investigated.

2. Experiment

In our experiment, ZnO NPs were synthesized from zinc acetate dehydrate (99.95% Fluka) precursor in methanol [18]. ZnO NPs were then transformed into a ZnO paste similar to the previous report [19]. Briefly, 5.0 g ZnO NPs were mixed with 8 ml HAc (0.1M) aqueous solution by mortar grinding. After being aged at room temperature, ZnO NPs were converted to a ZnO paste. The various metal (Ti, Al, Ag, Ni) substrates were prepared by e-beam evaporation of metals on glass in high vacuum. The porous ZnO films were fabricated by squeegee-printing the ZnO paste on metal substrates. For a bottom-illuminated DSC, the ZnO porous film was fabricated on the commercial FTO glass (Nipon Sheet Glass). After being dried at room temperature, the ZnO films were immersed in 0.3M ammonia for 15 min for surface activation. The activated films were cleaned with ethanol and dried in a laboratory oven. For dye loading, the ZnO films were immersed in an ethanol solution containing 0.3mM Ru-metal complex dye named D719 ($[RuL_2(NCS)_2]:2$ TBA) (from Everlight as a free sample) for 2 h. The transparent conducting GZO films as the counter electrode were deposited on glass substrates by a metal-organic chemical vapour deposition (MOCVD) system equipped with a home-made shower-head injector. Trimethylgallium (TMGa), dimethylzinc (DMZn) and oxygen were used as precursors and nitrogen was employed as a carrier gas for the metal-organics. The flow rates of N_2 and O_2 were controlled at 500 and 200 standard cubic centimetre per minute (sccm), respectively, while those of TMGa and DMZn were controlled both at 2 sccm. The GZO films were grown at a relatively low temperature of 300 °C with a chamber pressure of ∼25 Torr. The counter electrode was completed by sputtering Pt on the GZO film under mild conditions (20 mA) for 30 s. Some counter electrodes were also prepared on FTO for comparison. The two electrodes were bonded together by a ∼60 μm-thick thermal plastic. Finally, the electrolyte composed of 0.1M LiI, 0.5M terbutylpridine and 0.6M 1-hexyl-3-methylimidazolium iodide in methoxyacetonitrile was introduced between the electrodes by capillary action.

The photovoltaic measurement was conducted by illuminating the devices under a solar simulator (Model 16S-002, Solar Light Company Inc.) with a AM1.5G filter. The current–voltage (J–V) characteristics were studied using a Keithley 2400 sourcemeter. All devices were tested under ambient conditions and the simulated light intensity was adjusted to 100 mW cm^{-2} calibrated with a Thorlabs optical powermeter. The IPCE was measured by an IPCE measurement kit (Newport—Model QE-PV-SI) in dc mode. The scanning electron microscopy (SEM) images of ZnO porous film were recorded using a JEOL FESEM and the

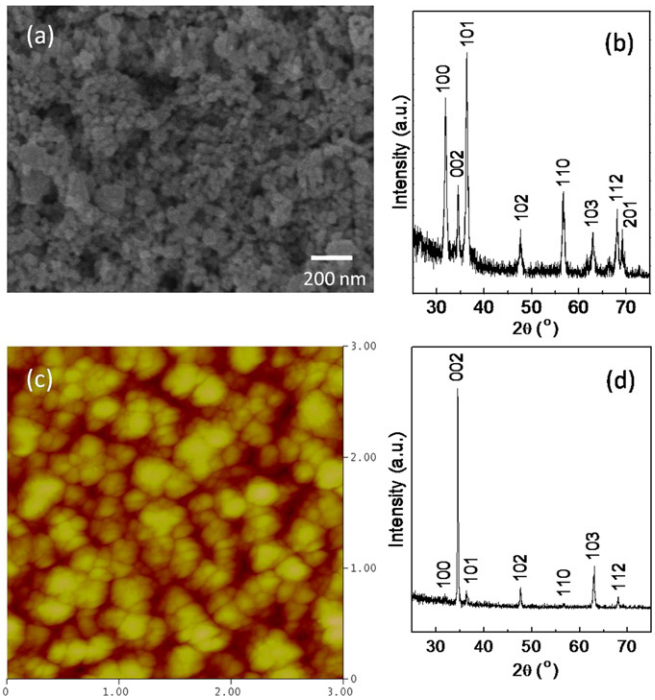

Figure 1. SEM image of ZnO porous film fabricated on Ti substrate (*a*) and its XRD pattern (*b*). AFM images of the GZO counter electrode deposited on glass substrate by MOCVD (the unit of scale bar is μm.) (*c*) and its XRD pattern (*d*).

tapping mode atomic force microscopy (AFM) images of the GZO film were taken with a Nanoscope IIIa (Digital Instruments) scanning probe microscope. X-ray diffraction (XRD) patterns of the films were obtained by a diffractometer (Siemens, model D5005) operating at 40 keV and 36 mA using Cu Kα (λ = 1.540 56 Å). The thickness of the films was measured by a surface profiler (KLA Tencor P-15). The sheet resistance and resistivity of GZO films were extracted using Hall effect measurement (BIO-RAD) with Van der Pauw geometry at room temperature. The optical transmittance and absorption spectra of the films were measured using a UV–Vis–NIR spectrophotometer system (PerkinElmer Lambda 950) with an integrating sphere to capture directly the transmitted light and forward scattered light.

3. Results and discussion

Figures 1(*a*) and (*b*) show the SEM images and XRD patterns of the porous ZnO film after surface activation. The average crystalline size of ZnO NPs both revealed from the SEM image and calculated from the XRD pattern using the Scherrer formula is about 20 nm. The thickness of the porous film is controlled at 8 μm. The film shows polycrystalline nature and all the diffraction peaks can be indexed to the hexagonal wurtzite structure of ZnO. There are two underlying mechanisms that promote the linkage between ZnO NPs as well as adhesion to the substrate: the surface charge effect and binder effect [19]. During the grinding process of the ZnO NPs in diluted HAc solution, the acid etches the surface of the ZnO NPs. The Ac^- ions screening on the surface of ZnO easily attract Zn^{2+} ions which come from the etching of ZnO by HAc. The etching process also generates $ZnAc_2$ which acts as a binder to connect ZnO NPs together as well as to anchor to the substrate. After the film has been dried, ammonia activation removes $ZnAc_2$ covered on the surface of the ZnO NPs easily without heating up to high temperatures by forming dissolvable $Zn(NH_3)_4^{2-}$, and the ZnO surface is changed to hydroxyl termination which facilitates the dye adsorption on the porous film.

Figures 1(*c*) and (*d*) show the AFM image and XRD patterns of the GZO film deposited by MOCVD. From AFM analysis, the roughness (rms) of the GZO film is ~25 nm. This nanoscale rough film also acts as an efficient anti-reflection coating due to the refractive index grading at the rough electrolyte/GZO interface [12]. As with the ZnO porous film, the hexagonal wurtzite structure of ZnO can be clearly seen in the resultant GZO film but no phase related to Ga is observed probably due to the low Ga content (~5 at%). A strong diffraction peak at $2\theta = 34.4^\circ$ indicates the preferential orientation along the (0 0 2) direction and high-quality crystallinity of the film. The resistivity of the GZO film measured by the Hall effect system is as low as $8.01 \times 10^{-4}\,\Omega$ cm. At the film thickness of ~750 nm, the sheet resistance of the film reaches 10.68 Ω/□.

The device architectures of a bottom-illuminated cell (conventional) and top-illuminated cell used in the experiment are illustrated in figure 2. The current–voltage (J–V) characteristics of DSCs with various working and counter electrodes both in the dark and under AM1.5G illumination (100 mW cm^{-2}) and the average values of their electrical parameters are shown in figure 3. In our discussion, we denote DSCs based on their working and counter electrodes, e.g. Ti–GZO refers to the DSC with Ti working electrode and Pt-coated GZO counter electrode. All devices, except the FTO–FTO device, are top-illuminated. The current density (J_{sc}) of Ti–GZO is similar to that of Ti–FTO; however, it drops by about 25% compared with the FTO–FTO bottom-illuminated device. The variation in J_{sc} can be understood by optical transmittance spectra of various electrodes and IPCE measurement (figure 4). The absorption edge of FTO is observed at 350 nm while that of GZO is shifted to 400 nm. The transmittance of GZO is, therefore, lower than that of FTO in the spectral region below 500 nm but the difference above 500 nm is smaller. The transmittance of both FTO and GZO films is slightly reduced upon Pt coating. Although a red shift in absorption edge occurred in GZO compared with FTO, this shift does not much affect the performance of the top-illuminated device due to the fact that the absorption edge of the electrolyte is at 480 nm. Hence, the transmittance of the combined GZO/Pt/electrolyte is comparable to that of the FTO/Pt/electrolyte and J_{sc} of the Ti–GZO device (4.756 mA cm^{-2}) is quite close to that of the Ti–FTO device (4.966 mA cm^{-2}). It is also observed that the IPCE spectrum of Ti–GZO is similar to that of the Ti–FTO device. The IPCE spectra of top-illuminated devices are not much different from those of bottom-illuminated devices at long wavelengths because of negligible absorption of electrolytes in this region. However, the transmittance of the GZO/Pt/electrolyte and the FTO/Pt/electrolyte is much lower than that of FTO in

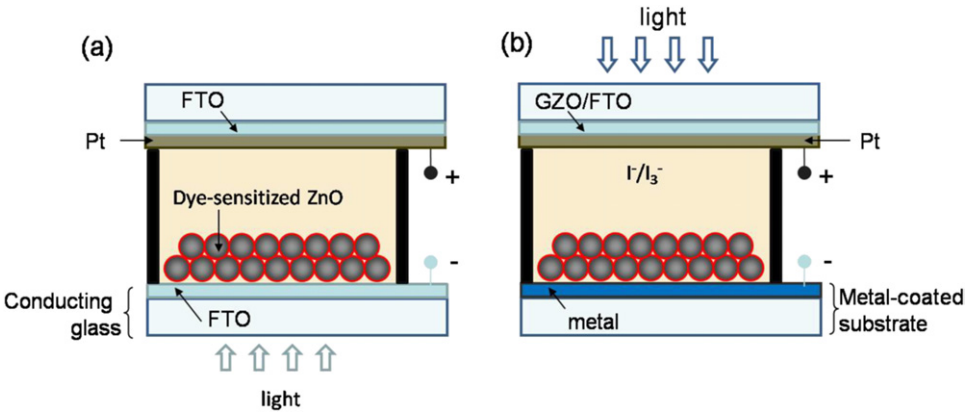

Figure 2. Schematic of bottom-illuminated cell (*a*) and top-illuminated cell (*b*).

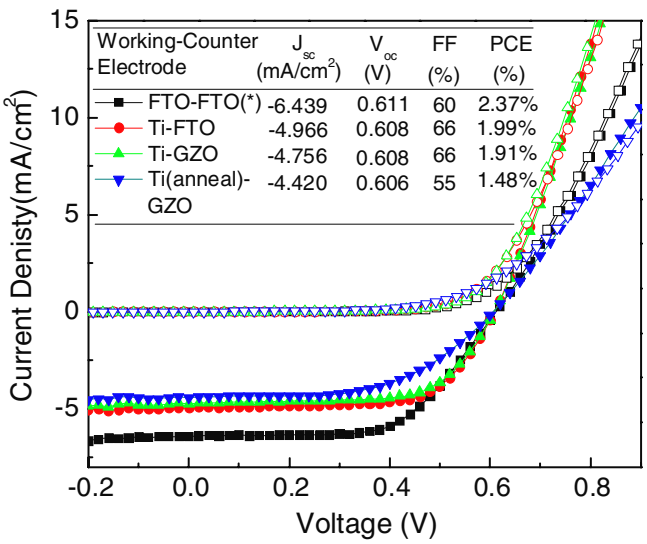

Figure 3. J–V characteristics of the bottom- and top-illuminated DSCs under illumination (filled symbols) and in the dark (open symbols). Devices are named in the format of working electrode–counter electrode. (*) denotes the bottom-illuminated device.

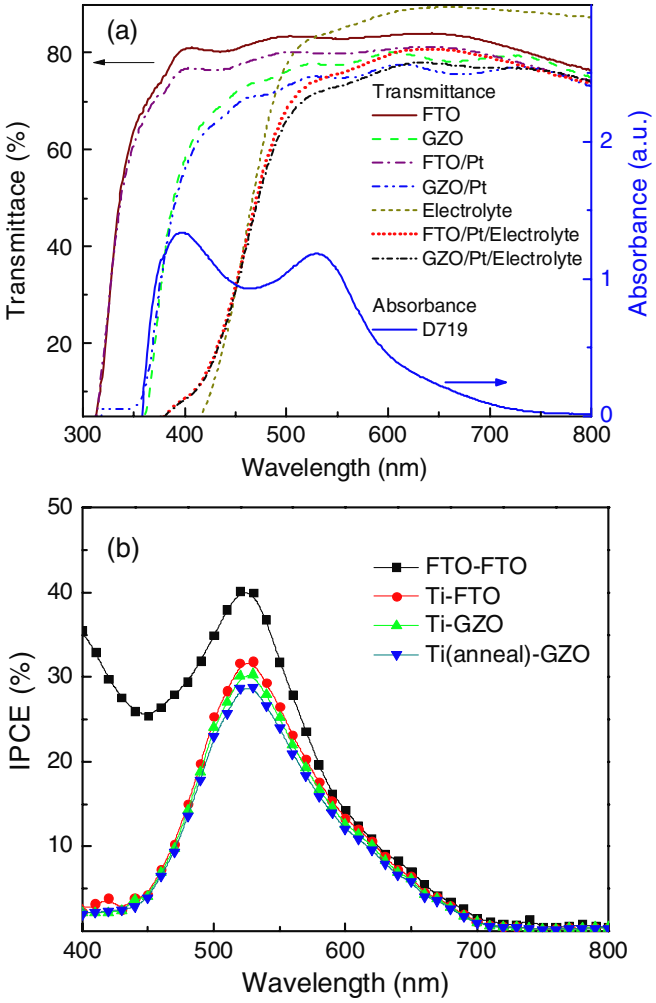

Figure 4. (*a*) Transmittance spectra of FTO and GZO with/without Pt and 60 μm-thick electrolyte (left vertical axis) and absorption spectrum of D719 dye (right vertical axis). (*b*) IPCE spectra of the fabricated devices.

the region below 500 nm due to the sharp absorption edge of the electrolyte around 480 nm. Therefore, in contrast to the bottom-illuminated device, the spectral responses of top-illuminated devices sharply drop below 500 nm and there is almost no observable response below 450 nm. The IPCE peaks of the top-illuminated devices are also affected due to this strong absorption of the electrolyte near its absorption edge. From IPCE and transmittance spectrum, we can conclude that the strong absorption of the electrolyte at the absorption edge (∼480 nm) is mainly responsible for a 20–25% drop in J_{sc} of the top-illuminated device.

The open circuit voltages (V_{oc}) of the fabricated devices are similar to each other but the fill factor (FF) of the devices with a Ti substrate (without anneal) (66%) is higher than that of the bottom-illuminated device with a FTO substrate (60%). Generally, FF of a solar cell is determined by two components: shunt resistance (R_{sh}) $[(dV/dI)_{V=0}]$ and series resistance (R_s) $[(dV/dI)_{V\geqslant V_{oc}}]$. It can be seen from the J–V curves that R_{sh} values of these devices are similar but Ti–FTO and Ti–GZO devices have smaller R_s than the FTO–FTO device. Therefore, higher FF of Ti–GZO and Ti–FTO devices can be attributed to a reduction in R_s, which can be explained by the energy band diagram at the ZnO and electrode interface. Figure 5(*a*) shows the energy levels of individual layers in the DSC before contact.

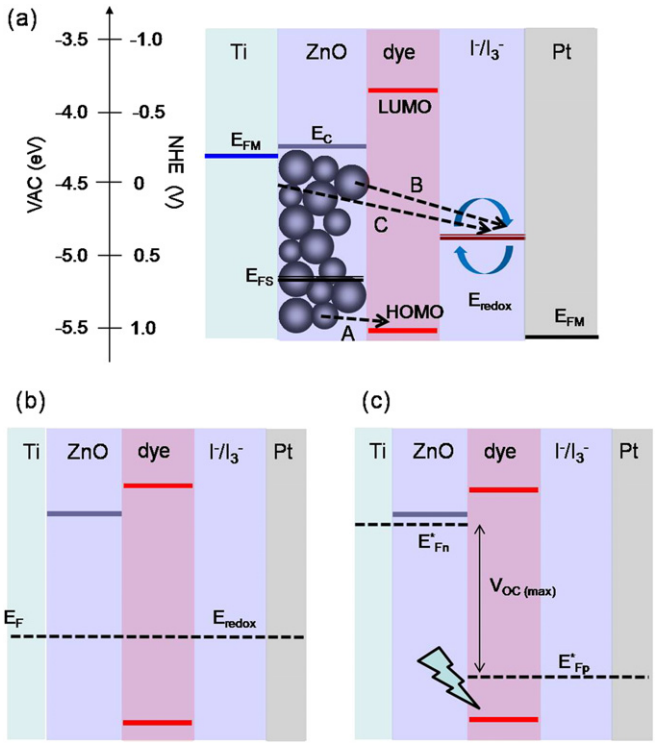

Figure 5. Schematic of top-illuminated DSC showing energetics of individual layers (*a*) before contact, (*b*) after contact in dark and (*c*) after contact under strong illumination and open circuit conditions. The vertical axis is the electron energy versus vacuum level (VAC) on the left scale and versus normal hydrogen electron (NHE) on the right scale. E_{FM}, E_C, E_{FS}, LUMO, HOMO and E_{redox} stand for Fermi level of metals, conduction band and Fermi level of ZnO (semiconductor), lowest unoccupied molecular orbital and highest occupied molecular orbital of dye and redox potential of electrolyte, respectively. E_F, E^*_{Fn} and E^*_{Fp} represent the Fermi level of the system (in the dark, equilibrium condition) and the quasi-electron and quasi-hole Fermi levels (under illumination, non-equilibrium condition). The vertical arrow in (*c*) indicates V_{oc} can be attained from the system. The energy levels are approximately drawn to scale. Dashed arrows A, B and C represent the recombination of injected electrons at ZnO/D^+, ZnO/ I_3^- and Ti/ I_3^- interfaces, respectively.

The work functions of metals are taken from the literature [20]. The electron affinity of ZnO is about 4.3 eV [21, 22], and the work function of the ZnO nanostructure, which is nearly independent of the geometrical size [23], is measured to be 5.2–5.3 eV [23–25]. In our analysis, the conduction band (E_C) and the Fermi level of the ZnO semiconductor (E_{FS}) are taken to be −4.29 eV and −5.2 eV with respect to the vacuum level, respectively. A redox potential of I^-/I_3^- electrolyte (E_{redox}) of −4.85 eV (with respect to the vacuum level) is extracted from the previous reports [26–28]. After ZnO is brought into contact with the liquid electrolyte in the dark, E_{FS} is aligned to E_{redox} as well as the Fermi level of metals (E_{FM}) of the two electrodes under equilibrium conditions (figure 5(*b*)). Band bending at the interfaces is neglected in this figure. Under strong illumination and open circuit conditions, this equilibrium condition is disturbed and E_{FS} moves up to the electron-quasi Fermi level (E^*_{Fn}), which is close to the conduction band minimum of ZnO due to the accumulation of photogenerated electrons in the E_C of ZnO (figure 5(*c*)). Likewise, E_{redox} is shifted to the hole-quasi Fermi level (E^*_{Fp}) owing to virtual hole injection into the electrolyte. The potential difference between E^*_{Fn} and E^*_{Fp} dictates the operating V_{oc} of the system.

Next we take a closer look at the energy levels across the interface between the electrodes and ZnO (figure 6(*a*)). The left diagram illustrates the energy level of Ti metal and ZnO semiconductor before contact. Upon contact and in the dark, the Fermi levels of Ti and ZnO are adjusted to I^-/I_3^- redox couple (−4.85 eV). Hence, the band bending of 0.87 eV and the band off-set of 0.04 eV appear at the interface. No band bending is formed at the metal side. The shift of E_C due to the solvation effects, which arise from immersion in the solvent [27], and Helmholtz layer dipole owing to the cation adsorption on the ZnO surface, which comes from the carboxylate group of the dye [27, 29], are ignored to simplify the discussion. Under strong illumination and open circuit conditions, E_F is shifted to E^*_{Fn} to be aligned with the Fermi level of Ti and an ohmic contact is then formed at the semiconductor and metal junction. On the other hand, the energetics of FTO and ZnO are different, as shown in figure 6(*b*). The work function of FTO is reported to be varied from 4.7 to 4.9 eV [27, 28, 30]. In our analysis, the work function of FTO is taken as 4.9 eV. Like the interface between Ti and ZnO, the Fermi levels of FTO and ZnO are aligned to −4.85 eV upon contact with the electrolyte under the dark condition. Band bendings of 0.3 eV and 0.61 eV are formed at the ZnO and FTO sides, respectively. Under strong illumination and open circuit conditions, in contrast to the Ti substrate, the alignment of the Fermi levels of FTO and E^*_{Fn} makes a Schottky contact at the metal and semiconductor junction, which obstructs electrons to be injected into the electrode. This Schottky barrier accounts for the increase in R_s of the FTO–FTO device whereas an ohmic contact is formed at the semiconductor/metal interface in the Ti–FTO/Ti–GZO devices and hence R_s decreases. On top of the ohmic contact, a very low sheet resistance of the Ti film (∼1.5 Ω/□), which is nearly an order of magnitude lower than that of FTO (14 Ω/□), also further reduces R_s, and in turn increases FF.

In our experiment, we also further deliberately annealed the working electrode (Ti substrate together with ZnO) at 450 °C in air to investigate the effect of high-temperature annealing. The FF of the Ti(anneal)–GZO device is dropped to 55% and J_{sc} is also slightly reduced. It is also observed that the sheet resistance of the Ti film increases to >300 Ω/□ (by two orders of magnitude) upon annealing due to oxidation of Ti. Therefore, we attribute this decrease in the FF to a high sheet resistance of the annealed film which increases R_s of the device. This clearly shows that we should adopt a low-temperature process for the top-illuminated DSC to avoid oxidation of metal (especially for low-work-function metals which can be easily oxidized) although the metal substrate withstands high temperatures.

From the J–V curves of the fabricated devices, we observe that V_{oc} is relatively constant despite electrode change. Generally the Fermi level shift in the semiconductor due to the accumulation of photogenerated electrons in the conduction band (in other words, the electron-quasi Fermi level shown as E^*_{Fn} in figure 5(*c*)) mainly determines V_{oc} of the resultant DSC

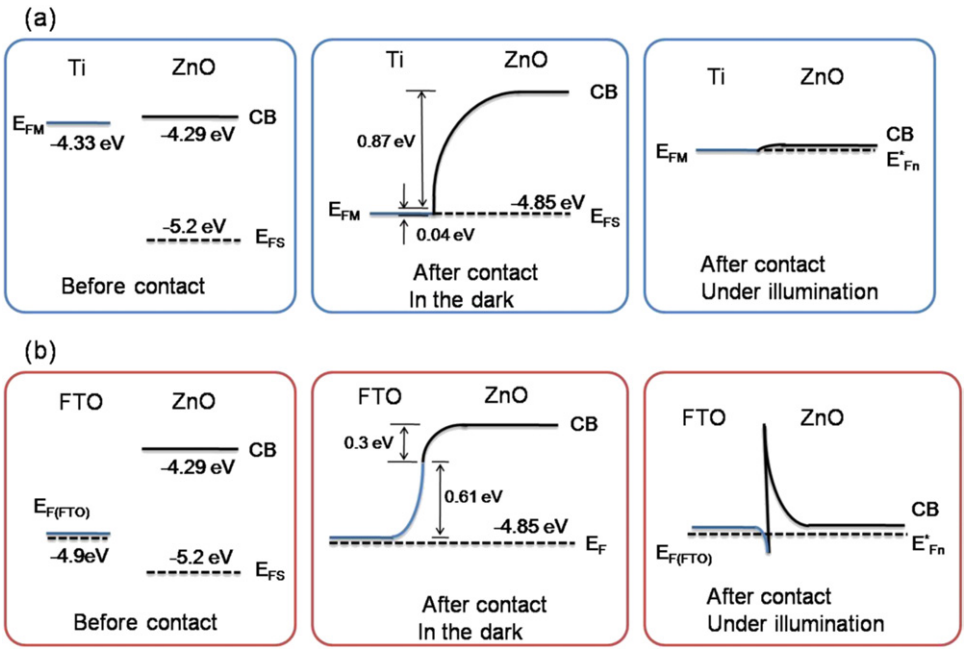

Figure 6. Schemes of electron energy at (*a*) Ti/ZnO contact and (*b*) FTO/ZnO contact. Left diagrams illustrate the energy level of individual layers before contact, centre ones show the band bending at the interface in the dark, and right diagrams show the formation of ohmic and Schottky contact for Ti/ZnO and FTO/ZnO, respectively, under strong illumination and open circuit conditions.

although some other limiting factors, including a large negative flat band potential of the electrode (FTO) [28] and band edge displacement [31], are suggested. As E^*_{Fn} depends on the electron concentration in the semiconductor, V_{oc} should be related to the recombination of injected electrons with oxidized dye (D^+) or I_3^- ions—either at the interface of ZnO/dye (A), ZnO/electrolyte (B) or Ti(FTO)/electrolyte (C), as shown in figure 5(*a*). Since the net current flow at V_{oc} is zero, V_{oc} can be worked out by equating the electron injection current density and the recombination current density at bias $V = V_{oc}$ [31]. Mathematically it can be expressed as

$$V_{oc} = \frac{kT}{q} \ln\left(\frac{AI}{n_0 k_1 [D^+] + n_0 k_2 [I_3^-] + n_{e0} k_3 [I_3^-]}\right),$$

where k is the Boltzmann constant, T denotes the temperature, q represents the fundamental charge; k_1, k_2 and k_3 are the kinetic constants of recombination for A, B and C, respectively; n_0 and n_{e0} are the concentrations of the electronic states in the semiconductor and electrode in the dark (equilibrium); $[D^+]$ and $[I_3^-]$ are the concentrations of the oxidized dye and oxidized redox couple; and A and I are the area of the electrode and incident photon flux, respectively. Differently from previous reports [31–33], we include the recombination at the electrode/redox couple interface in our expression and ignore the reaction order for I_3^- and electron as it is close to 1 [26]. Because the recombination processes A and B are the same for both top- and bottom-illuminated devices and V_{oc} is relatively constant for all devices, it can be concluded that the recombination between the electrode and I_3^- is not worsened by replacing FTO with Ti. This hypothesis can be supported by the J–V curves of which the inverse slopes at zero bias are similar for the top- and bottom-illuminated devices. This observation also refutes the previous suggestion that the large negative flat band potential of FTO limits the maximum attainable V_{oc} because an increase in V_{oc} is not observed although the negative flat band potential is reduced by replacing FTO with Ti [28].

We also investigated the effect of metal substrate on the performance of top-illuminated DSCs by employing various metals with different work functions (from low to high). We used Al, Ti, Ag and Ni (whose work functions are 4.18 eV, 4.33 eV, 4.74 eV and 5.35 eV, respectively) [20] as the working electrode and Pt-coated GZO as the counter electrode. J–V characteristics of the fabricated devices are depicted in figure 7(*a*). Only a very small photovoltaic effect is generated from the Al device (inset of figure 7(*a*)) although a favourable ohmic contact between Al and ZnO was reported [34]. Therefore, we suppose that an oxide layer is formed between Al and ZnO owing to the easily oxidizable nature of Al. The oxidation process makes the work function of Al even lower than that of pristine Al [35]. The work function of Al is reported to be reduced to −3.7 eV after being exposed to air in 1 h [35], and the work function of its oxide film is reported to be as low as −1.6 eV [36]. This low-work-function oxide layer creates a huge barrier for electrons at the conduction band of ZnO to flow to Al electrode, and hence only a small amount of photocurrent is extracted. However, Ag and Ni devices have a reasonable photovoltaic effect despite a lower performance than the Ti device. As seen from the J–V curves, R_{sh} of the Ti device is much higher than that of the Ag and Ni devices, suggesting that there is less recombination in the Ti device compared with the Ag and Ni devices. Because the same materials, except for the bottom electrode metal, are used in all devices, the recombination rates of A and B (refer to figure 5(*a*)) are the same in all devices. A poor performance of Ag and Ni devices can, therefore, be attributed to the recombination of

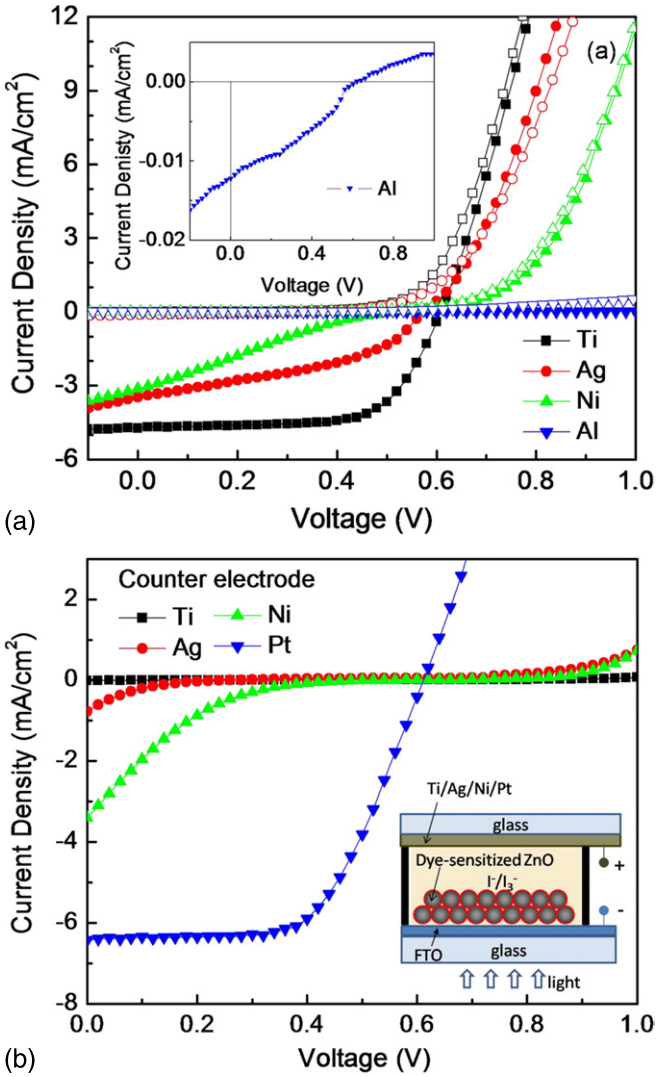

Figure 7. (*a*) *J*–*V* characteristics of top-illuminated devices with various metal substrates (Al, Ti, Ag and Ni) under illumination (filled symbols) and in the dark (open symbols). Inset: *J*–*V* curve of Al device at low scale to show the small photovoltaic effect. Pt-coated GZO is used as the counter electrode in these devices. (*b*) *J*–*V* characteristics of bottom-illuminated devices with various counter electrodes (Ti, Ag, Ni and Pt) to investigate the catalytic effect of the metals. Inset: device architecture used to test the catalytic effect.

injected electrons with oxidized I_3^- ions at the metal/electrolyte interface (recombination C). To confirm this hypothesis, we investigated the catalytic activity for redox reaction of the metals by fabricating bottom-illuminated DSCs with these metals as the counter electrode and Pt-counter electrode as a reference (figure 7(*b*) inset). The *J*–*V* characteristics of these devices are shown in figure 7(*b*). When Ti is used as the counter electrode, no photovoltaic effect is observed, meaning that Ti exhibits very little or no catalytic activity. However, we observed photovoltaic effect when Ag and Ni are used as the counter electrode. Hence, Ag and Ni exhibit catalytic activity although their effect is not as strong as Pt. When Ag and Ni are used as the working electrode in the top-illuminated device, the catalytic property of these metals enhances the reaction $I_3^- + 2e \rightarrow 3I^-$ at the working electrode/electrolyte interface and increases the recombination of injected electrons with reducing I_3^-. As Ni has a higher catalytic effect than Ag, the FF of the Ni device is lower than that of the Ag device. The recombination current also has a negative impact on the photogenerated current, and hence J_{sc} of Ag and Ni devices are smaller than that of the Ti device. As discussed previously, V_{oc} of the DSC depends logarithmically on the inverse of kinetic constant of recombination; the increase in recombination also reduces V_{oc}. Therefore, we observed the descending order of V_{oc} from the Ti to the Ni device. Another factor for the inferior performance of Ag and Ni devices is the high work function of the metal. Like FTO, high-work-function Ag and Ni result in a Schottky barrier at the ZnO/metal junction under strong illumination and open circuit conditions, hence increasing R_s. When the device operates as a diode in the dark, high-work-function Ni creates a higher barrier than Ti or Ag does. The turn-on voltage of the Ni device is, therefore, higher than that of Ti and Ag devices in the dark *J*–*V* curves. In fact, Ag is not suitable to be used as an electrode because we noticed that Ag film is corroded within an hour after injecting the liquid electrolyte (as it is vulnerable to the corrosive iodide/triiodide redox electrolyte). However, we did not observe any corrosion on Ti metal by visual inspection even after a few weeks. These findings reveal that Ti is a more appropriate metal to be used in top-illuminated devices.

In summary, we demonstrated FTO/ITO-free, top-illuminated DSCs with room-temperature-processed ZnO photoanodes on Ti substrates. The efficiency of such a top-illuminated DSC with a GZO counter electrode (1.91%) is comparable to that of conventional DSCs with the commercial FTO counter electrode (1.99%). Although the efficiency of the top-illuminated DSC is about 20% lower than the conventional bottom-illuminated DSC (2.37%), it reduces the cost of DSC by eliminating the use of conventional conducting glass (FTO/ITO), which is the most expensive part of a DSC. Our room-temperature-processed photoanode yields a higher fill factor than the high-temperature-processed photoanode without sacrificing the good interconnection between nanoparticles and adhesion to the substrate. We also showed that Ti is more suitable to be used in a top-illuminated DSC architecture than other metals because of minimum catalytic activity on redox reactions and high resistance to corrosion.

Acknowledgments

This work was supported by the Ministry of Education, Singapore, under the Academic Research Fund (RGM 44/06), NRF-RF-2009-09 and NRF-CRP-4-2008-04.

References

[1] Nazeeruddin M K, De Angelis F, Fantacci S, Selloni A, Viscardi G, Liska P, Ito S, Takeru B and Grätzel M 2005 *J. Am. Chem. Soc.* **127** 16835

[2] Fang X, Ma T, Akiyama M, Guan G, Tsunematsu S and Abe E 2005 *Thin Solid Films* **472** 242

[3] Karthik S, Mor G K, Prakasam H E, Yoriya S, Paulose M, Varghese O K and Grimes C A 2007 *Nanotechnology* **18** 065707

[4] Varghese O K, Paulose M and Grimes C A 2009 *Nature Nanotechnol.* **4** 592
[5] Chen Q and Xu D 2009 *J. Phys. Chem.* C **113** 6310
[6] Andrei G, Sergiu P A, Jan M M and Patrik S 2008 *Small* **4** 1063
[7] Kang M G, Park N-G, Ryu K S, Chang S H and Kim K-J 2006 *Sol. Energy Mater. Sol. Cells* **90** 574
[8] Onoda K, Ngamsinlapasathian S, Fujieda T and Yoshikawa S 2007 *Sol. Energy Mater. Sol. Cells* **91** 1176
[9] Tan W, Yin X, Zhou X, Zhang J, Xiao X and Lin Y 2009 *Electrochim. Acta* **54** 4467
[10] Ito S, Ha N-L C, Rothenberger G, Liska P, Comte P, Zakeeruddin S M, Pechy P, Nazeeruddin M K and Gratzel M 2006 *Chem. Commun.* 4004
[11] Minami T 2008 *Thin Solid Films* **516** 1314
[12] Hüpkes J, Müller J and Rech B 2008 *Transparent Conductive Zinc Oxide* ed K Ellmer, A Klein and B Rech (Berlin: Springer) p 359
[13] Müller J *et al* 2001 *Sol. Energy Mater. Sol. Cells* **66** 275
[14] Yoshida Y, Tanaka S, Hiromitsu I, Fujita Y and Yoshino K 2008 *Japan. J. Appl. Phys.* **47** 867
[15] Chen H *et al* 2008 *Semicond. Sci. Technol.* **23** 045004
[16] Fortunato E, Assunção V, Gonçalves A, Marques A, Águas H, Pereira L, Ferreira I, Vilarinho P and Martins R 2004 *Thin Solid Films* **451–452** 443
[17] Zhao J, Sun X W and Tan S T 2009 *IEEE Trans. Electron Devices* **56** 2995
[18] Claudia P, Andreas K and Horst W 2002 *Angew. Chem. Int. Edn* **41** 1188
[19] Liu X, Luo Y, Li H, Fan Y, Yu Z, Lin Y, Chen L and Meng Q 2007 *Chem. Commun.* 2847
[20] Skriver H L and Rosengaard N M 1992 *Phys. Rev.* B **46** 7157
[21] Ho Y M, Zheng W T, Li Y A, Liu J W and Qi J L 2008 *J. Phys. Chem.* C **112** 17702
[22] Sanghyun J, Sunkook K, Saeed M, David B J, Young-Geun H, Antonio F and Tobin J M 2008 *Appl. Phys. Lett.* **92** 022104
[23] Bai X, Wang E G, Gao P and Wang Z L 2003 *Nano Lett.* **3** 1147
[24] Xudong W, Christopher J S and Zhong Lin W 2005 *Appl. Phys. Lett.* **86** 013111
[25] Lee C J, Lee T J, Lyu S C, Zhang Y, Ruh H and Lee H J 2002 *Appl. Phys. Lett.* **81** 3648
[26] Boschloo G and Hagfeldt A 2009 *Acc. Chem. Res.* **42** 1819
[27] Cahen D, Hodes G, Gratzel M, Guillemoles J F and Riess I 2000 *J. Phys. Chem.* B **104** 2053
[28] Turrión M, Bisquert J and Salvador P 2003 *J. Phys. Chem.* B **107** 9397
[29] Schlichthorl G, Huang S Y, Sprague J and Frank A J 1997 *J. Phys. Chem.* B **101** 8141
[30] Wei X, Xie T, Xu D, Zhao Q, Pang S and Wang D 2008 *Nanotechnology* **19** 275707
[31] Huang S Y, Schlichthorl G, Nozik A J, Gratzel M and Frank A J 1997 *J. Phys. Chem.* B **101** 2576
[32] Wang Q, Moser J-E and Grätzel M 2005 *J. Phys. Chem.* B **109** 14945
[33] Lee K, Park S W, Ko M J, Kim K and Park N-G 2009 *Nature Mater.* **8** 665
[34] Kim H K and Lee J M 2007 *Superlatt. Microstruct.* **42** 255
[35] Semov Y I 1969 *Phys. Status Solidi* b **32** K41
[36] Antula J 1966 *Solid-State Electron.* **9** 825